# Plug-and-play measurement of chromatic dispersion by means of two-photon interferometry

Romain Dalidet, Anthony Martin, Mattis Riesner, Sidi-Ely Ahmedou, Romain Dauliat, Baptiste Leconte, Guillaume Walter, Grégory Sauder, Jean-Christophe Delagnes, Guy Millot, et al.

# Plug-and-Play Measurement of Chromatic Dispersion by Means of Two-Photon Interferometry

Romain Dalidet,[1] Anthony Martin,[1] Mattis Riesner,[1] Sidi-Ely Ahmedou,[2] Romain Dauliat,[2] Baptiste Leconte,[2] Guillaume Walter,[3] Grégory Sauder,[1] Jean-Christophe Delagnes,[3] Guy Millot,[4,5] Philippe Roy,[2] Raphaël Jamier,[3] Sébastien Tanzilli,[1] and Laurent Labonté[1,*]

[1] *Université Côte d'Azur, CNRS, Institut de physique de Nice, France*

[2] *Université de Limoges, CNRS, XLIM, UMR 7252, Limoges F-87000, France*

[3] *Centre Lasers Intenses et Applications (CELIA), Université de Bordeaux-CNRS-CEA, UMR 5107, Talence Cedex F-33405 , France*

[4] *ICB, Université de Bourgogne, CNRS, UMR 6303, Dijon F-21078, France*

[5] *Institut Universitaire de France (IUF), 1 Rue Descartes, Paris, France*

(Received 6 March 2023; revised 24 May 2023; accepted 21 July 2023; published 10 August 2023)

Since the first proof-of-principle experiments 25 years ago, quantum metrology has matured from fundamental concepts to versatile and powerful tools in a large variety of research branches, such as gravitational-wave detection, atomic clocks, plasmonic sensing, and magnetometry. At the same time, two-photon interferometry, which underpins the possibility of entanglement to probe optical materials with unprecedented levels of precision and accuracy, holds the promise to stand at the heart of innovative functional quantum sensing systems. We report a quantum based method for measuring the frequency dependence of the velocity in a transparent medium, i.e., chromatic dispersion (CD). This technique, using energy-time-entangled photons, allows straightforward access to CD value from the visibility of two-photon fringes recorded in a free-evolution regime. In addition, our quantum approach features all the advantages of classical measurement techniques, i.e., flexibility and accuracy, all in a plug-and-play system.

DOI: 10.1103/PhysRevApplied.20.024026

## I. INTRODUCTION

Quantum metrology applies quantum physics for precise measurements, despite challenges in the fragility of quantum systems. It aims to estimate parameters using quantum features, offering improved performance over classical methods. Physical platforms such as cold atoms, nitrogen-vacancy centers, and superconducting circuits enable accurate measurements of time, accelerations, rotations, gravity, and magnetic fields [1–5]. Photons, with their mobility and advanced manipulation techniques, are an appealing quantum system [6–8]. Recent advancements in generating quantum photonic states enhance metrology tasks in various domains. Photonic quantum correlations boost quantum sensor performance [8].

Since many physical problems can be regarded as phase-estimation processes, two-photon interferometry represents one of the most relevant approaches, notably for the measurement of dispersive properties such as chromatic dispersion (CD) [9]. The measurement of CD holds significant relevance in numerous applications within the field of photonics, particularly in classical [10] and quantum communications [11], as well as the generation of nonlinear effects [10], encompassing platforms based on $\chi^{(2)}$ and $\chi^{(3)}$ nonlinearities. To date, the measurement of CD has been achieved using two main categories of techniques, relying on the spectral or temporal properties of the light probe. On the one hand, temporal CD measurements exhibit a great flexibility but require the use of a spectrally broad light source and a picosecond-time-resolution detector over a kilometer length, resulting in moderate accuracy [12]. On the other, interferometric techniques enable measurements with an excellent accuracy over the widest spectral range, at the cost of (i) a complex experimental setup, including a spectrometer, (ii) systematic errors, and (iii) a moderate signal-to-noise ratio [13]. Even if quantum enhancement of accuracy has recently been demonstrated, the process is still rather tedious, time consuming, and difficult to automate [14].

In this work, we propose an original approach among current CD measurement methods that merges the best aspects of classical techniques with unique quantum features, in a plug-and-play fashion system associated with a 1% accuracy. This method relies on the distinctive

*laurent.labonte@univ-cotedazur.fr

 

properties of photonic entanglement through two-photon interference. We highlight three advantages: (i) the method relies on recording the free evolution of the interference fringes and so neither a spectrometer nor a stabilization system are required; (ii) the CD value is obtained directly due to an elegant formalism that infers the CD coefficient directly from the visibility of the two-photon interference; and (iii) this free-alignment method is definitively oriented toward real-world applications.

## II. THEORETICAL FRAMEWORK

Frequency-entangled photons generated via spontaneous parametric down-conversion (SPDC) can be described by the two-photon state

$$|\psi(t)\rangle \propto \iint d\omega_s d\omega_i \alpha(\omega_s+\omega_i)\Gamma(\omega_s,\omega_i)\hat{a}_s^+(\omega_s)\hat{a}_i^+(\omega_i)|0\rangle, \tag{1}$$

where the subscripts $s$ and $i$ denote signal and idler photons, respectively. $\eta$, $\alpha$, and $\Gamma$ represent the strength of the nonlinear interaction, the complex amplitude of the pump spectrum (approximated by a Dirac function in the continuous regime), and the spectral distribution of the photon pair, i.e., the phase-matching function, respectively. $\omega_i$ and $\omega_s$ fulfill the energy conservation. The revelation of the entanglement carried by this biphoton state lies in the two-photon interference through an appropriate unbalanced interferometer, often referred to as a Franson configuration [15,16]. It should be noted that in our case, we regard the two-photon state propagating within the interferometer as equivalent to an N00N state, achieved through post-selection during detection [17,18]. The visibility of the two-photon interference depends on the indistinguishability of the two paths in term of losses, polarization, and spatial modes, as well as CD. More specifically, considering Taylor expansion of the wave vector around the degeneracy wavelength, odd-order terms of the dispersion vanish due to energy conservation [19] associated with SPDC. The phase accumulated by the quantum state propagating within the interferometer can be expressed as

$$\phi = L\sum_{j=s,i}\sum_{n=0}^{\infty}\frac{\Omega_j^n}{n!}\beta_j^{(n)} = L\left(2\beta^{(0)}+\beta^{(2)}\Omega^2\right)+O(\Omega^4), \tag{2}$$

where $\beta^{(n)} = \partial k/\partial\omega|_{\omega_0}$, $\Omega$, and $L$ denote the different orders of the propagation constant, the detuning from the center frequency $\omega_0$, and the length of the sample under test (SUT), respectively. The initial term, $\beta^{(0)}$, denotes a straightforward phase shift, whereas the subsequent term, $\beta^{(2)}$, defines the group velocity, from which we can establish the CD through a simple linear relationship [10]. By performing a careful analysis of the evolution of the photon pair within the interferometer, using Eqs. (1) and (2), the visibility of the fringes reads

$$V = \left[\left(\int_{-\infty}^{\infty} d\Omega|\Gamma(\Omega)|^2\cos(\beta^{(2)}\Omega^2 L)\right)^2 + \left(\int_{-\infty}^{\infty} d\Omega|\Gamma(\Omega)|^2\sin(\beta^{(2)}\Omega^2 L)\right)^2\right]^{1/2}, \tag{3}$$

where $\int_{-\infty}^{\infty} d\Omega|\Gamma(\Omega)|^2) = 1$ (see Appendixes A and B for details). The evolution of the visibility depends highly on the spectral-distribution shape of the photon pairs, as shown in Fig. 1, where Gaussian and square shapes are considered. In the case of a normalized Gaussian-distributed spectrum, i.e.,

$$|\Gamma(\Omega)|^2 = \frac{1}{\sigma\sqrt{2\pi}}e^{\frac{-1}{2}(\frac{\Omega}{\sigma})^2},$$

with spectral width $\sigma$, the visibility can be written in the analytic form (see Appendix B for detail):

$$V = \frac{1}{\sqrt[4]{\gamma^2+1}}, \tag{4}$$

where $\gamma = 2\sigma^2\beta^{(2)}L$ represents an adimensional parameter carrying all the information on the dispersion (the sample length $L$, spectral bandwidth $\sigma$, and dispersion-coefficient value $\beta^{(2)}$). This simple form indicates a straightforward relation between the visibility and the CD parameter. In other words, when the photon pair probes an object, information about the dispersive behavior of this object is imprinted on the two-photon state. This direct access to CD appears as a unique feature, as temporally based CD measurements usually give access to the group delay before inferring the CD parameter. It is important to note that the sensitivity to $\gamma$ depends on the spectral profile of the photon pairs, as also shown in Fig. 1. The highest sensitivity is obtained when the leading coefficient of the tangent is maximum, i.e., at the inflection point. Considering only positive values of $\gamma$, the latter is located at the (only) inflection of the curve, where the second-order derivative is null:

$$\frac{\partial^2 V}{\partial\gamma^2} = \frac{3\gamma^2-2}{4(\gamma^2+1)^{9/4}} \Leftrightarrow \gamma = \sqrt{\frac{2}{3}}, \tag{5}$$

corresponding to a visibility of $V = (5/3)^{-1/4} \approx 0.88$.

In summary, assuming a Gaussian spectral distribution, direct access to the CD parameter is granted due to the precise knowledge of the visibility, which stands as a parameter that is easily accessible experimentally, without the need for a spectrometer or an active stabilization system.

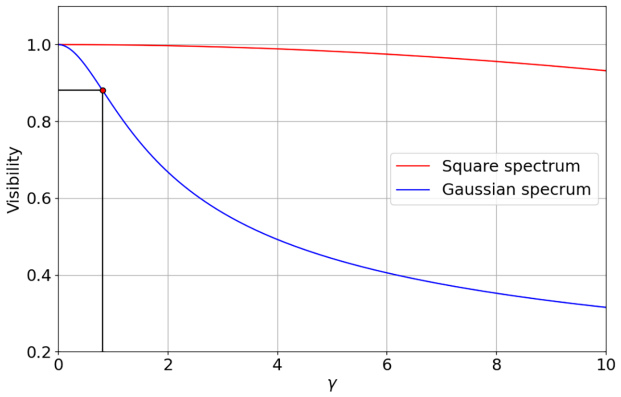


FIG. 1. The visibility of the two-photon interference ($V$) as a function of the parameter $\gamma$, assuming square (Gaussian) functions represented by the red (blue) curves, respectively. The red dot shows the inflection point from Eq. (5).

## III. TWO-PHOTON INTERFERENCE VISIBILITY ESTIMATION

In most optical experiments, stabilization of the interferometric system is of the utmost importance in order to acquire precise and accurate measurements. However, many environmental parameters (e.g., temperature, pressure, and vibration) impact the final result, requiring fine control. In interferometric systems, both passive and active stabilization are often considered. For passive stabilization, interferometers are placed in a hermetically sealed case with thermal feedback. While this method is easy to implement, short- and long-term thermal drift cannot be managed in the same way, thus excluding a high degree of accuracy and long runs. On the other hand, active stabilization, which is commonly based on an error signal generated from the output of the interferometer and fed back to a phase-compensating mechanism in one of its arms, is more robust against any kind of variations, at the cost of more expensive and more complex apparatus (e.g., a narrow-linewidth and stable laser and a wavelength demultiplexer). Here, we show theoretically and experimentally an interferometric method based on the free evolution of two-photon interference, avoiding the use of spectrometer and stabilization systems.

Figure 2 shows a diagram of the general principle of our method. The coincidence probability at the output of the interferometer is given by

$$P_c(\phi) \propto \frac{1}{2}\left[1 + V\cos(\phi + \phi_0)\right], \tag{6}$$

where $\phi_0$ and $V$ represent an offset and the visibility of the two-photon interference, respectively,

$$V = \frac{C_{\max} - C_{\min}}{C_{\max} + C_{\min}}, \tag{7}$$

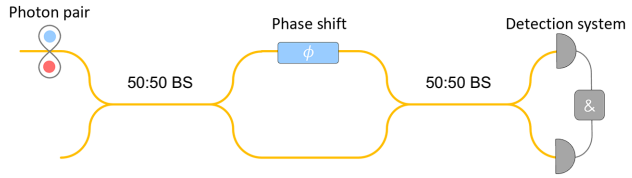


FIG. 2. A photon pair experiences a Mach-Zehnder interferometer in which a phase shifter $\phi$ is introduced. At the output beam splitter (BS), the two beams interfere, creating interference patterns. The detection system comprises two single-photon detectors and a time-to-digital converter (TDC) for detecting coincidences.

in which $C_{\max}$ and $C_{\min}$ are the maximum and minimum coincidence rates, respectively. The cumulative distribution function (CDF) is defined as the cumulative density of the variable $\phi$, $F(x) = P_c(\phi) < P_c(x)$:

$$F(x) = \frac{\operatorname{asin}(\frac{2}{V}(x - \frac{1}{2}))}{\pi} + \frac{1}{2}. \tag{8}$$

This function increases monotonically and gives the probability that the parameter $\phi$ will take a value below $x$. The probability density function (PDF), $f(x)$, which therefore sets the visibility likelihood for a distribution of coincidences, is defined as the derivative of the aforementioned function $F(x)$:

$$f(x) = \frac{2}{\pi V\sqrt{1 + \frac{-4x^2+4x-1}{V^2}}}. \tag{9}$$

Thus, a free drift of the phase provides access to the PDF, from which we deduce the visibility and then the CD. The photon pairs follow Poisson-type statistics and we will assess its impact on the measurements. In order to illustrate this formalism, we simulate the effect of a Poissonian statistic on the parameter estimation $V$ and the PDF through Eq. (9). As shown in Fig. 3, we set the two-photon interference visibility to 0.75 with, on average, 100 [Fig. 3(a)] and 1000 [Fig. 3(b)] photon pairs. The red curves represent the theoretical prediction without a finite statistic and the yellow and blue filled curves represent the spread due to the Poissonian distribution for 100 and 1000 photon pairs, respectively. The PDF functions, presented in Figs. 3(c) and 3(d), show that the probabilities are very close to the extreme values of 0.125 and 0.875 (corresponding to a visibility $V = 0.75$) as most of the possible values spread over the extremes. The Poissonian statistic of the detection induces modifications of the PDF: (i) the edges spread over the two extreme values and (ii) an asymmetry arises between these two extreme values. The first behavior emerges naturally from the Poissonian noise, while the second one comes from the asymmetry of the Poissonian distribution $\gamma = \lambda^{\frac{1}{2}}$, where $\lambda$ denotes the

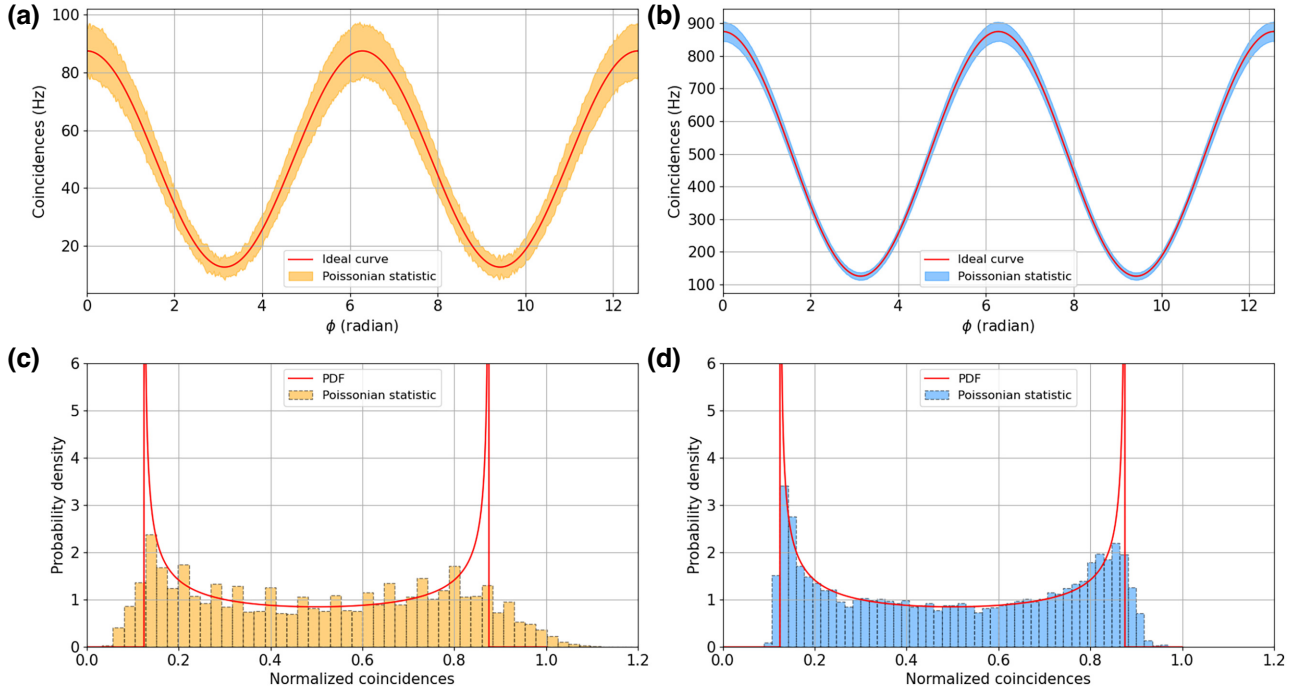


FIG. 3. (a),(b) The simulated Eq. (6) with $V = 0.75$ and (a) $P_c(\max) = 100$ (a) and (b) $P_c(\max) = 1000$. Filled curves represent the statistical fluctuation due to the Poissonian distribution of the detection. (c),(d) The theoretical probability density function described by Eq. (9) (red curve). The histograms are generated using Eq. (6) for $N = 10^4$ occurrences, with $\phi \in [0, 2\pi]$ randomly distributed. The (c) orange and (d) blue histograms refer to (a) and (b), respectively.

parameter of the Poissonian distribution. In other words, the relative error of the distribution is inversely proportional to the number of events. This model clearly shows the necessity of considering a high coincidence rate ($> 10^3$) to mitigate the impact of the statistic.

We employ two complementary approaches to measuring CD. They are based on Eq. (4), where the key parameter lies in the extraction of visibility, which we establish using the PDF. In one case, we operate at the inflection point and acquire the PDF by allowing the phase to drift. In another case, we reconstruct Fig. 1 with multiple values of $\gamma$.

Our approach based on the exploitation of the two-photon interference is reminiscent of the seminal violation of Bell's inequality applied to the interferometric—also called the Franson—configuration in the 1980s [15]. This interferometric technique used to measure the quantum correlation induced by energy-time entanglement [16] and has opened the way to a wide range of applications such as nonlocal dispersion cancellation to ensure the security of Franson-based quantum key distribution protocols [20–22]. All cases require precise knowledge of the visibility. Two strategies are primarily exploited. The first one relies on Eq. (7), where the extreme points $C_{\max}$ and $C_{\min}$ are inferred from the data analysis. On the other hand, the interference pattern can be fitted by Eq. (6). As the offset always fluctuates over the acquisition time, only the first oscillations are considered. None of the established methods were convincing enough, as they consider only a part of the statistics. By contrast, we highlight the relevance of our approach, which relies on the acquisition of long sets of data, each one being part of the PDF function. By the way, all the statistics contribute to precise knowledge of the $V$ parameter.

## IV. EXPERIMENTAL RESULTS

A continuous wave (CW) laser (Toptica TA Pro) emitting at a wavelength of 780.23 nm is directed through a polarization controller, followed by a pigtailed type-0 periodically poled lithium niobate (PPLN) waveguide. This configuration is employed to generate frequency-correlated photon pairs through a spontaneous down-conversion (SPDC) process, occurring on both sides of the degenerate wavelength $\lambda_0 = 1560.46$ nm, as illustrated in Fig. 4. The phase-matching condition of the nonlinear interaction is fine-tuned to produce photon pairs whose spectral shape is of a "flat top" type, centered at the degeneracy wavelength. The pairs are then shaped using a filter to obtain a Gaussian spectrum centered around twice the pump-laser wavelength (see Fig. 5). The photon pairs travel along a fiber-based interferometer where the sample under test (SUT) is a standard SMF-28 fiber. Faraday mirrors are placed at the output of

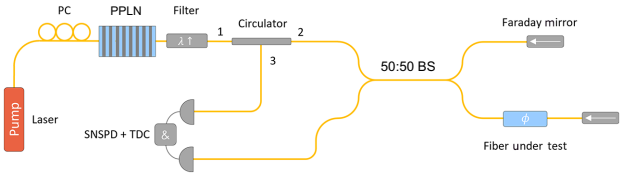


FIG. 4. The experimental setup. A cw laser pumps a periodically poled lithium niobate (PPLN) waveguide from which correlated photon pairs are emitted via SPDC. These pairs are spectrally shaped with a filter before passing through a Michelson interferometer. Coincidence counts are registered using superconducting nanowire single-photon detectors (SNSPDs) and a TDC. BS, 50:50 beam splitter; PC, polarization controller.

each arm, ensuring mode-polarization indistinguishability. Finally, coincidences are recorded using superconducting-nanowire single-photon detectors (SNSPDs) and a time-to-digital converter (TDC). At the output of the Michelson interferometer, the two photon contributions following the same path are indistinguishable and therefore preserved, while the satellite contributions resulting from the propagation of photons along different paths are discarded using the TDC [16].

As our method relies on the acquisition of the interference operating in a free-running regime, a careful analysis has to be carried out to ensure that the bandwidth of the detection system is higher than the phase drift.

From the temperature-dependent refractive index of fused silica, corresponding to $\Delta n/n \approx 4.8.10^{-6}.\mathrm{K}^{-1}.\Delta T$, where $\Delta T$ represents the temperature shift in kelvin [23], the sensitivity for a standard fiber can be extracted and is 0.2 K/m per fringe, which corresponds to a variation

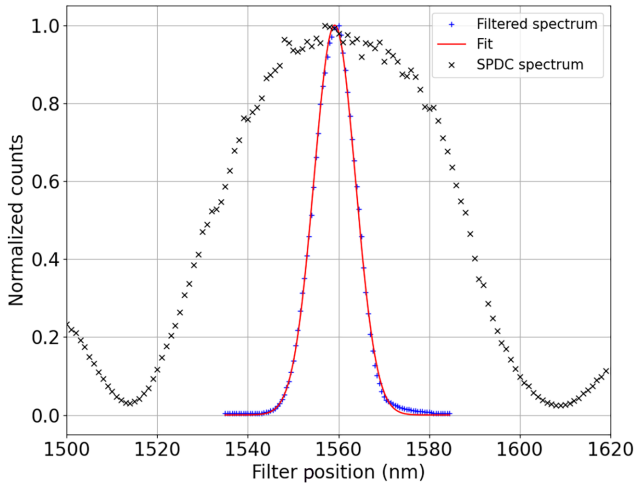


FIG. 5. The spectrum of the photon pairs. The black dotted curve corresponds to the natural spectrum of the pairs. The blue dotted curve is the spectrum measured after the band-pass filter. The red curve is a fit of the latter, from which we extract a width of $\sigma = 4.57$ nm. SPDC, spontaneous down-conversion.

of 45 mK in the case of a 2.4-m-long fiber. By acquiring the temperature of the experiment room over 10 h, the Fourier transform of the latter shows that typical variations have an amplitude of approximately 35 mK and a frequency $f \in [0.5, 2]$ Hz, which is consistent with a 100-ms acquisition time.

We set out two different strategies for measuring the CD parameter. We extract the visibility: (i) at a fixed operating point $\gamma$, corresponding to the inflection point (see Fig. 1, whereupon Eq. (4) is reversed to infer the parameter $\gamma$ from $V$; or (ii) for different values of $\gamma$ corresponding to different spectral bandwidths of the filter, fitted by Eq. (4).

For both approaches, a prerequisite has to be fulfilled to guarantee that the CD is the only factor impacting the visibility, ruling out other distinguishability criteria as differential losses and/or spatial, time, and polarization modes. A calibration is fulfilled by measuring a 100% visibility by considering narrow filtering, ensuring that all the latter criteria are satisfied.

### A. Method based on the inflection point

Regarding Fig. 3, we need to make a trade-off concerning the pump-power regime: a high number of coincidences ensuring that the statistics tend to the PDF, while maintaining a double-pair generation rate low enough not to deteriorate the visibility (typically $< 0.01$ pairs per window of interest), due to accidental coincidences. The pump power is set to generate a maximum coincidence rate of $P_c \approx 10^4$ Hz, while the full width at half maximum (FWHM) of the Gaussian filter is set to 4.5 nm, giving a visibility close to 0.88, in accordance with the inflection point of Eq. (4). The raw spectrum out of the PPLN and the Gaussian-like filtered spectrum are shown in Fig. 5.

Typical two-photon fringes drifting in a free-running regime are shown in Fig. 6(a). A histogram is built from a set of 500 points (50s) in Fig. 6(b), and then is fitted according to Eq. (9). As expected, the PDF is shaped by the inherent Poissonian statistic. While the relative error induced by a Poissonian distribution is lower for high values, the absolute error is smaller for low values. In order to minimize the fitting error induced by the distribution, only the left part of the histogram is used [see Fig. 6(c)], where the absolute error is the smallest. Then, Eq. (4) is reversed to extract the CD. After 200 measurements (Fig. 7), we obtain a CD parameter of 17, 1(2) ps/(km nm).

### B. Method based on multiple operating points

The CD parameter is extracted by fitting Eq. (4). Two scenarios are possible to tune the parameter $\gamma$ over the $x$ axis in Fig. 1: either the length of the sample or the spectral bandwidth of the filter. This latter parameter is easily accessible, as most of band-pass filter can be made tunable, thus strengthening our vision of a user-friendly demonstrator. The length of the sample will be such that

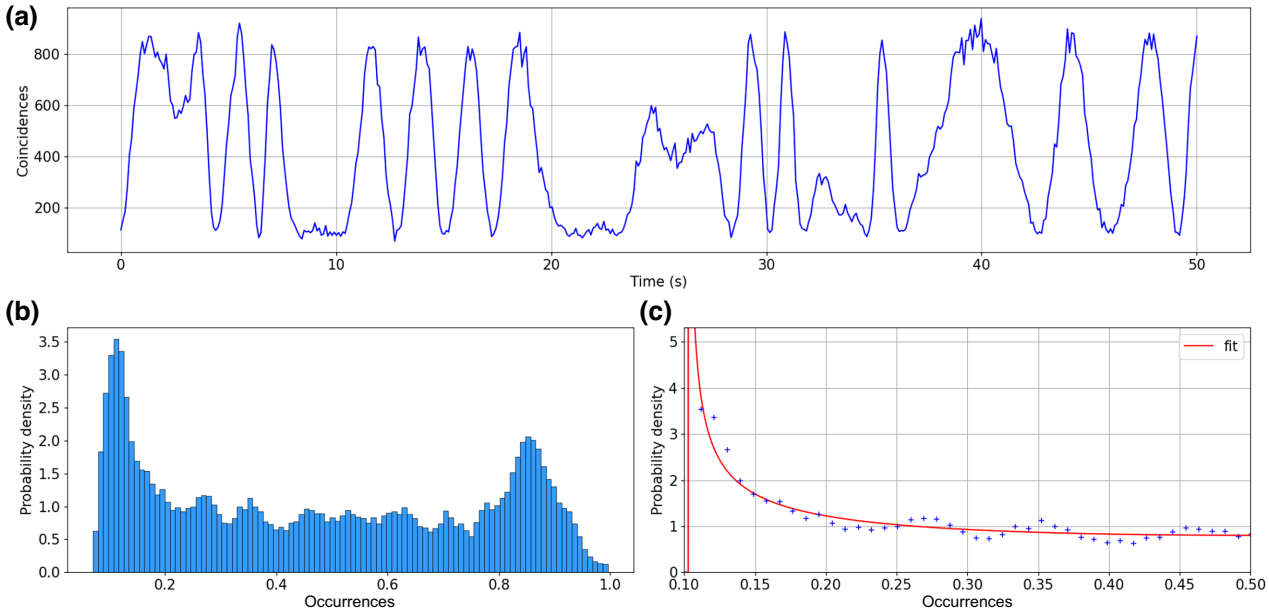


FIG. 6. (a) The acquired coincidences (the central peak of the Franson histogram) as a function of time. (b) The histogram extracted from the acquired data. (c) The fitted curve (red) of the left part of (b), using Eq. (9).

the visibility curve can be described with standard tunable filters, the spectral bandwidth of which ranges from approximately 0.1 nm to approximately 10 nm. According to Fig. 1, the length of the sample is set to 4.5 m. As in the previous method, a calibration is undertaken prior to any measurement, ensuring 100% visibility by considering narrow filtering. To keep the same Poissonian statistic with respect to the different spectral bandwidth, the pump power is increased as the bandwidth of the filter is reduced, so that the maximum number of coincidences remains the same, $P_c \approx 10^4$ Hz. The number of points acquired as well as the procedure of the visibility extraction remain identical to the first method, described in Sec. III.

Figure 8 shows the visibility values associated with each filter spectral width. The graph is fitted using Eq. (4) with the only free parameter being the CD parameter, leading to a CD value equal to 17.2(2) ps/(km nm).

The values of the CD parameter are 17.1(2) ps/(km nm) and 17.2(2) ps/(km nm) for both methods. Both approaches give results that are consistent, each of them within 1% of precision, and also with the manufacturer's data, which predict a value $\leq 18$ ps/(km nm) [24]. We would have

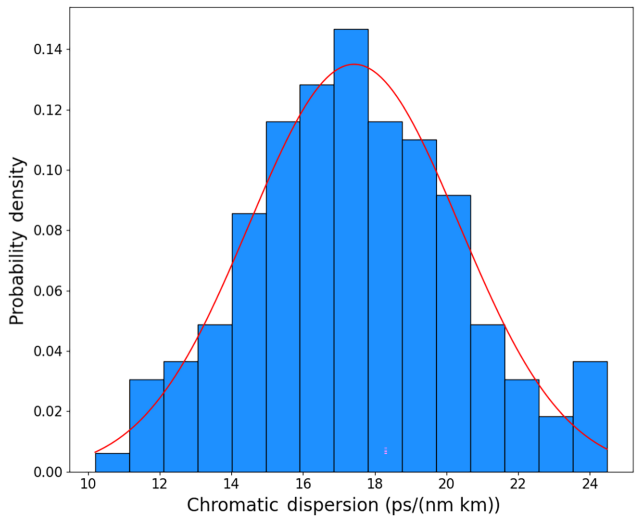


FIG. 7. The CD measurement from 200 data samples (blue histogram) and its Gaussian fit (red).

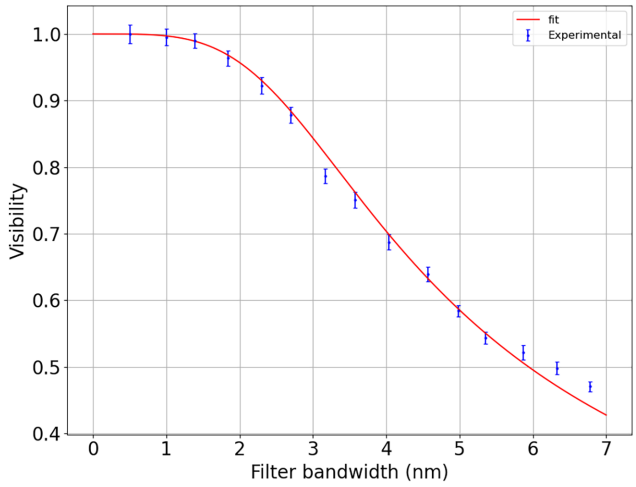


FIG. 8. The extracted visibility as a function of the filter bandwidth. The number of measurements for each point is 200.

TABLE I. A comparison between the various CD-measurement techniques. WLI, white-light interferometry; QWLI, quantum white-light interferometry.

| Method | CD accuracy (%) | Sample length | Active stabilization | Dedicated equipment |
|---|---|---|---|---|
| Phase shift [25] | 0.1 | km | No | Standard |
| Time of flight [26] | 3 | m | No | Standard |
| WLI [27] | 1.5 | [cm; m] | Yes | Spectrometer and balanced interferometer |
| QWLI [14] | 0.02 | [cm; m] | Yes | Spectrometer |
| Our work | 1 | [cm; m] | No | Standard |

expected that the first method would have given a better precision as it relies on the most-sensitive sensitive point, whereas the second method implements points with different sensitivities. This intuition has to be mitigated by a most-favorable statistic, because a higher number of runs has been performed for the second method: 3000 instead of 200 measurements.

In Table I, we summarize the main characteristics of the different CD-measurement methods, including both classical and quantum approaches. Even if accuracy appears as a primary factor of importance for a measurement technique, other criteria should be considered. Exhibiting a precision on the CD parameter below 1% is required for nonlinear effects that are sensitive to a higher order of dispersion $\beta_i$ (with $i \geq 2$), such as four-wave mixing or modulation instability. But in most telecommunication network cases, such a precision is not necessary, whereas friendly-user, practical, and intuitive techniques are preferred, which explains the prevalence of CD apparatus based on temporal methods in the industry. Our approach demonstrates a trade-off among the different methods, allowing us to exhibit high accuracy while retaining simple implementation with direct access to the dispersion due to the unique features of quantum photonics. Our approach, based on free-running acquisition and combining the simplicity of temporal methods with the accuracy of spectral methods, has the potential to compete with well-established conventional techniques. Beyond the measurement of CD, this method opens up a new application path, that of probing the dispersive properties of materials, in the same way as distance measurement for optical coherence tomography or transmission or absorption for spectroscopy.

## V. DISCUSSION AND CONCLUSIONS

We have implemented a new technique for measuring the CD through a direct relation between the visibility of the two-photon interference and the CD parameter, based on the assumption of a Gaussian profile of the two-photon states. This model goes beyond the scope of probing dispersive properties in material and could be useful for a wide variety of applications that require accurate knowledge of the visibility, such as to ensure security for quantum key distribution protocols. The key point of our technique is to gather the simplicity of implementation of temporal techniques associated with the high accuracy of spectral ones, without the requirement of active stabilization. We have shown that our technique is compliant with two complementary variations, resulting in a similar 1%. This work represents a step toward a realistic and a friendly-user quantum enhanced demonstrator, which outperform the classical counterparts (in terms of accuracy, reproducibility, and immunity to the environment) that have been demonstrated so far over the past 20 years. Our strategy focuses on a specific use case in this present work but has to be included in a more general framework, within the acceleration of quantum technologies, of the new generation of quantum enhanced sensors that are emerging from the laboratories.

The data are available from the authors upon reasonable request.

## ACKNOWLEDGMENTS

This work has been conducted within the framework of the project OPTIMAL ("Automated Maskless Laser Lithography Platform for First Time Right Mixed Scale Patterning"), funded by the European Union by means of the Fond Européen de développement regional (FEDER). We also acknowledge financial support from the Agence Nationale de la Recherche (ANR), through the projects Quantum metrology for near- to mid-infrared photonic applications, the CNRS through its program "Mission interdisciplinairité," under the project labeled Quantum metrology for fine refractive index measurement, and the French government, through its Investments for the Future program, under the Université Côte d'Azur UCA-JEDI project (Quantum@UCA) managed by the ANR (ANR-15-IDEX-01).

M.R. established the theory and R.D. and G.S. performed the experiments under the supervision of A.M. All of the authors contributed to the paper.

The authors declare that there are no competing interests.

## APPENDIX A: EVOLUTION OF TWO-PHOTON STATE THROUGH AN INTERFEROMETER

The creation operator $a^\dagger$, located at the input of the interferometer, undergoes an evolution described by $a^\dagger \rightarrow$

$1/\sqrt{2}(a^\dagger + b^\dagger)$ upon encountering the first beam splitter. Here, $a^\dagger$ and $b^\dagger$ denote the paths corresponding to the lower and upper arms of the interferometer, respectively. The operators $c^\dagger$ and $d^\dagger$ represent the two output modes emerging from the interferometer, at the output of the second beam splitter. The phase that each photon accumulates when traversing the arm containing the SUT is denoted as $\Phi_{a,b}(\omega)$. This phase function can be expanded around a central frequency, specifically $\omega_0 = \omega_{\text{pump}}/2$:

$$\Phi_i(\omega) = L_i \sum \frac{\partial^n \beta_i}{\partial \omega^n} \frac{(\omega_0 - \omega)^n}{n!} = L_i \sum \beta_i^{(n)} \frac{\Omega^n}{n!}, \quad \text{(A1)}$$

where $L$ denotes the length of the arm containing the SUT. $\beta^{(0)}$, $\beta^{(1)}$, and $\beta^{(2)}$ represent the distinct orders, namely a simple phase shift, the inverse of the group velocity, and the group-velocity dispersion, respectively. The evolution within the interferometer is governed by the following equation:

$$a_{\text{in}}^\dagger \rightarrow \frac{1}{2}\left[(e^{i\Phi_a(\omega)} + e^{i\Phi_b(\omega)})c^\dagger + (e^{i\Phi_a(\omega)} - e^{i\Phi_b(\omega)})d^\dagger.\right] \quad \text{(A2)}$$

Photon pairs are generated through SPDC, as described in Sec. IV. As a result of spectral filtering, these pairs are introduced into the interferometer through the input mode $a$. Their behavior can be characterized by the two-photon state 1. In the following, the evolution through the interferometer is considered:

$$\begin{aligned}|\psi_{\text{in}}\rangle \propto \frac{1}{4}\iint d\omega_{s,i}\Gamma(\omega_s,\omega_i)\left[(e^{i\Phi_a(\omega_s)} + e^{i\Phi_b(\omega_s)})c_s^\dagger\right.\\ + (e^{i\Phi_a(\omega_s)} - e^{i\Phi_b(\omega_s)})d_s^\dagger\Big]\\ \times\left[(e^{i\Phi_a(\omega_i)} + e^{i\Phi_b(\omega_i)})c_i^\dagger\right.\\ \left. + (e^{i\Phi_a(\omega_i)} - e^{i\Phi_b(\omega_i)})d_i^\dagger\right]|0\rangle, \end{aligned} \quad \text{(A3)}$$

$$\begin{aligned}|\psi_{\text{out}}\rangle \propto \frac{1}{4}\iint d\omega_{s,i}\Gamma(\omega_s,\omega_i)\left[(e^{i\Phi_a(\omega_s)} + e^{i\Phi_b(\omega_s)})(e^{i\Phi_a(\omega_i)}\right.\\ + e^{i\Phi_b(\omega_i)})c_s^\dagger c_i^\dagger\\ + (e^{i\Phi_a(\omega_s)} - e^{i\Phi_b(\omega_s)})(e^{i\Phi_a(\omega_i)} - e^{i\Phi_b(\omega_i)})d_s^\dagger d_i^\dagger\\ + (e^{i\Phi_a(\omega_s)} + e^{i\Phi_b(\omega_s)})(e^{i\Phi_a(\omega_i)} - e^{i\Phi_b(\omega_i)})c_s^\dagger d_i^\dagger\\ \left. + (e^{i\Phi_a(\omega_s)} - e^{i\Phi_b(\omega_s)})(e^{i\Phi_a(\omega_i)} + e^{i\Phi_b(\omega_i)})d_s^\dagger c_i^\dagger\right]|0\rangle. \end{aligned} \quad \text{(A4)}$$

At the output of the Michelson interferometer, the identical paths taken by two photon contributions render them indistinguishable. Conversely, the satellite contributions arising from the traversal of photons along disparate paths are discarded by postselection [16].

## APPENDIX B: COINCIDENCE PROBABILITY AT THE OUTPUT OF AN INTERFEROMTER, DESCRIPTION AND INTERPRETATION

The probability of coincidence, denoted as $P_c$, is determined by the projection of the output state $|\psi_{\text{out}}\rangle$ onto the state $c_{\omega'}^\dagger d_{\omega''}^\dagger|0\rangle = |\omega_c\omega_d'\rangle$. This state represents the detection of a single photon at frequency $\omega$ in output mode $c$ and another photon at frequency $\omega'$ in output mode $d$. The coincidence probability can be considered identical to

$$P_c = \iint d\omega d\omega' \left|\langle\omega_c\omega_d'|\psi_{\text{out}}\rangle\right|^2, \quad \text{(B1)}$$

where the integration encompasses the monochromatic modes that are received by the detectors. By utilizing the commutation relation $[c_\omega, c_{\omega'}^\dagger] = \delta(\omega - \omega')$ and taking into account the symmetry of $G = G(\omega_s,\omega_i) = G(\omega_i,\omega_s)$, Eq. (B1) can be simplified as follows:

$$\begin{aligned}P_c = \frac{1}{8}\iint d\omega d\omega' |\Gamma(\omega,\omega')|^2 \left|(e^{i\Phi_a(\omega)} + e^{i\Phi_b(\omega)})(e^{i\Phi_a(\omega')}\right.\\ \left. - e^{i\Phi_b(\omega')})\right|^2. \end{aligned} \quad \text{(B2)}$$

By introducing the substitutions $\omega = \omega_0 + \Omega$ and $\omega' = \omega_0 - \Omega$, and reorganizing the phase functions $\phi_{a,b}(\omega)$ to create a global phase term, we can express Eq. (B2) as follows:

$$\begin{aligned}P_c &= \frac{1}{8}\int d\Omega |\Gamma(\Omega)|^2 \left|(1 + e^{i\phi(\Omega)})(1 - e^{i\phi(-\Omega)})\right|^2\\ &= \frac{1}{2}\int_{-\infty}^{\infty} d\Omega |\Gamma(\Omega)|^2 [1 + \cos(\Phi(\Omega)) - \cos(\Phi(-\Omega))\\ &\quad - \cos(\Phi(\Omega))\cos(\Phi(-\Omega))]. \end{aligned} \quad \text{(B3)}$$

The expression $\cos(\Phi(\Omega)) - \cos(\Phi(-\Omega))$ exhibits odd behavior, irrespective of the specific form of $\Phi(\Omega)$. Conversely, the function $|\Gamma(\Omega)|^2$ demonstrates evenness or symmetry. As a consequence, the quantity $|G'(\Omega)|^2[(\cos(\Phi(+\Omega)) - \cos(\Phi(-\Omega)]$ also possesses odd characteristics, resulting in a zero integral across the entire frequency spectrum. On the contrary, the term $\cos(\Phi(\Omega))\cos(\Phi(-\Omega))$ is even and contributes to the variable $P_c$. By employing trigonometric product-to-sum identities, we can express it as

$$\begin{aligned}\cos(\Phi(\Omega))\cos(\Phi(-\Omega)) = \frac{1}{2}\cos[\Phi(\Omega) + \Phi(-\Omega)]\\ + \frac{1}{2}\cos[\Phi(\Omega) - \Phi(-\Omega)].\end{aligned}$$

This separation enables us to isolate the even component $((\Phi(\Omega) + \Phi(-\Omega))/2)$ and the odd component

$((\Phi(\Omega) - \Phi(-\Omega))/2)$ of $\Phi(\Omega)$. Consequently, Eq. (B3) assumes the following form:

$$P_c = \frac{1}{4}\int d\Omega|\Gamma(\Omega)|^2 \{2 - \cos[\Phi(\Omega) + \Phi(-\Omega)] - \cos[\Phi(\Omega) - \Phi(-\Omega)]\} \tag{B4}$$

$$= \frac{1}{4}\left\{2 - \int d\Omega|\Gamma(\Omega)|^2 \cos[\Phi(\Omega) + \Phi(-\Omega)] - \int d\Omega|\Gamma(\Omega)|^2 \cos[\Phi(\Omega) - \Phi(-\Omega)]\right\}. \tag{B5}$$

In order to understand what each term in Eq. (B5) is describing, we primarily neglect the second- and higher-order terms of the dispersion:

$$P_c = \frac{1}{4}\left\{2 - \int d\Omega|\Gamma(\Omega)|^2 \cos[2\beta^{(0)}L] - \int d\Omega|\Gamma(\Omega)|^2 \cos[2\Omega\beta^{(1)}L]\right\} \tag{B6}$$

$$= \frac{1}{4}\left\{2 - \cos(2\beta^{(0)}L) - \hat{G'} \star \hat{G}(2\beta^1 L)\right\}, \tag{B7}$$

where $\hat{G(t)} = \int_{-\infty}^{\infty} d\Omega\Gamma(\Omega)\cos[\Omega t] = \int_{-\infty}^{\infty} d\Omega\Gamma(\Omega)e^{i\Omega t}$ denotes the Fourier transform of $\Gamma(\Omega)$ and $\hat{G} \star \hat{G}(t) = \int_{-\infty}^{\infty} ds\hat{G(s)}G^*(\hat{s-t})$ the autocorrelation of $\hat{G}$.

This represents the well-established interferogram of a two-photon state, where the first component accounts for all distinguishable paths available, the second component arises when two photons (the N00N state, with $N = 2$) traverse the same path, resulting in Franson-type interference, and the third component corresponds to the interference between two identical monochromatic modes, reminiscent of the Hong-Ou-Mandel (HOM) effect.

Upon the incorporation of second- and third-order dispersion into our model, the integration of Eq. (B7) becomes more complex. The term associated with the Franson type can now be formulated as follows:

$$F = \int d\Omega|\Gamma(\Omega)|^2 \cos[\Psi(\Omega) + \Psi(-\Omega)] \tag{B8}$$

$$= \int d\Omega|\Gamma(\Omega)|^2 \cos[2\beta^{(0)}L + \beta^{(2)}\Omega^2 L] \tag{B9}$$

$$= \int d\Omega|\Gamma(\Omega)|^2 \left[\cos(2\beta^{(0)}L)\cos(\beta^{(2)}\Omega^2 L) - \sin(2\beta^{(0)}L)\sin(\beta^{(2)}\Omega^2)L\right] \tag{B10}$$

$$= \cos(2\beta^{(0)}L) \cdot \int d\Omega|\Gamma(\Omega)|^2 \cos(\beta^{(2)}\Omega^2 L) - \sin(2\beta^{(0)}L) \cdot \int d\Omega|\Gamma(\Omega)|^2 \sin(\beta^{(2)}\Omega^2 L) \tag{B11}$$

$$= V_D \cdot \cos(2\beta^{(0)}L + \psi_D), \tag{B12}$$

where

$$\psi_D = \tan^{-1}\left(\frac{\int d\Omega|\Gamma(\Omega)|^2 \sin(\beta^{(2)}\Omega^2 L)}{\int d\Omega|\Gamma(\Omega)|^2 \cos(\beta^{(2)}\Omega^2 L)}\right), \tag{B13}$$

$$V_D = \sqrt{\left(\int d\Omega|\Gamma(\Omega)|^2 \cos(\beta^{(2)}\Omega^2 L)\right)^2 + \left(\int d\Omega|\Gamma(\Omega)|^2 \sin(\beta^{(2)}\Omega^2 L)\right)^2} \tag{B14}$$

are the phase and the visibility of the oscillation. Using the Cauchy-Schwarz inequality, one can find that $V_D \leq 1$ but the exact value is highly dependent on the spectrum $\Gamma(\Omega)$.

Assuming a Gaussian distribution for the spectrum with a bandwidth denoted as $\sigma$, one can calculate the visibility and phase of the oscillation as a function of $\gamma = 2\sigma^2\beta^{(2)}L$. This parameter, which combines the spectral width and CD, allows for the evaluation of the visibility and phase:

$$\int d\Omega|\Gamma(\Omega)|^2 \cos(\beta^{(2)}\Omega^2 L) = \sqrt{\frac{1 + \sqrt{1 + \gamma^2}}{2 + 2\gamma^2}} \tag{B15}$$

$$\int d\Omega |\Gamma(\Omega)|^2 \sin(\beta^{(2)}\Omega^2 L) = \frac{\gamma}{\sqrt{2(1+\gamma^2)(1+\sqrt{1+\gamma^2}}}. \tag{B16}$$

Finally, Eq. (B14) thus becomes

$$V_D = \frac{1}{\sqrt[4]{\gamma^2+1}}. \tag{B17}$$


[1] R. Schirhagl, K. Chang, M. Loretz, and C. L. Degen, Nitrogen-vacancy centers in diamond: Nanoscale sensors for physics and biology, Annu. Rev. Phys. Chem. **65**, 83 (2014).

[2] R. Geiger, A. Landragin, S. Merlet, and F. Pereira Dos Santos, High-accuracy inertial measurements with cold-atom sensors, AVS Quantum Sci. **2**, 024702 (2020).

[3] J. M. Taylor, P. Cappellaro, L. Childress, L. Jiang, D. Budker, P. R. Hemmer, A. Yacoby, R. Walsworth, and M. D. Lukin, High-sensitivity diamond magnetometer with nanoscale resolution, Nat. Phys. **4**, 810 (2008).

[4] C. Degen, F. Reinhard, and P. Cappellaro, Quantum sensing, Rev. Mod. Phys. **89**, 035002 (2017).

[5] J. Clarke and F. K. Wilhelm, Superconducting quantum bits, Nature **453**, 1031 (2008).

[6] M. A. Taylor and W. P. Bowen, Quantum metrology and its application in biology, Physics Reports Quantum Metrology Application Biology **615**, 1 (2016).

[7] M. I. Kolobov, The spatial behavior of nonclassical light, Rev. Mod. Phys. **71**, 1539 (1999).

[8] A. S. Clark, M. Chekhova, J. C. F. Matthews, J. G. Rarity, and R. F. Oulton, Special Topic: Quantum sensing with correlated light sources, Appl. Phys. Lett. **118**, 060401 (2021).

[9] J. G. Rarity, J. Burnett, P. R. Tapster, and R. Paschotta, High visibility two photon interference in a single mode fibre interferometer, Europhysics Letters (EPL) **22**, 95 (1993).

[10] G. P. Agrawal, *Nonlinear Fiber Optics*, Optics and photonics (Academic Press, San Diego, California, 1995), 2nd ed.

[11] S. Fasel, N. Gisin, G. Ribordy, and H. Zbinden, Quantum key distribution over 30 km of standard fiber using energy-time entangled photon pairs: a comparison of two chromatic dispersion reduction methods, Eur. Phys. J. D **30**, 143 (2004).

[12] *Proc.23rd Int. Symposium on Distributed Computing*, Lecture Notes in Computer Science, Vol. 5805 (Springer-Verlag, Berlin, 2009).

[13] L. Labonte, P. Roy, D. Pagnoux, F. Louradour, C. Restoin, G. Mélin, and E. Burov, Experimental and numerical analysis of the chromatic dispersion dependence upon the actual profile of small core microstructured fibres, J. Opt. A: Pure Appl. Opt. **8**, 933 (2006).

[14] F. Kaiser, P. Vergyris, D. Aktas, C. Babin, L. Labonte, and S. Tanzilli, Quantum enhancement of accuracy and precision in optical interferometry, Light: Sci. Appl. **7**, 17163 (2018).

[15] J. D. Franson, Bell Inequality for Position and Time, Phys. Rev. Lett. **62**, 2205 (1989).

[16] D. Aktas, B. Fedrici, F. Kaiser, T. Lunghi, L. Labonte, and S. Tanzilli, Entanglement distribution over 150 km in wavelength division multiplexed channels for quantum cryptography, Laser Photon. Rev. **10**, 451 (2016).

[17] C. Autebert, N. Bruno, A. Martin, A. Lemaître, C. Gomez Carbonell, I. Favero, G. Leo, H. Zbinden, and S. Ducci, Integrated AlGaAs source of highly indistinguishable and energy-time entangled photons, Optica **3**, 143 (2016).

[18] D. Oser, S. Tanzilli, F. Mazeas, C. Alonso Ramos, X. Le Roux, G. Sauder, X. Hua, O. Alibart, L. Vivien, E. Cassan, and L. Labonte, High quality photonic entanglement out of a stand-alone silicon chip, npj Quantum Inf. **6**, 31 (2020).

[19] A. Riazi, E. Y. Zhu, C. Chen, A. V. Gladyshev, P. G. Kazansky, and L. Qian, Alignment-free dispersion measurement with interfering biphotons, Opt. Lett. **44**, 1484 (2019).

[20] V. Scarani, H. Bechmann-Pasquinucci, N. J. Cerf, M. Dušek, N. Lütkenhaus, and M. Peev, The security of practical quantum key distribution, Rev. Mod. Phys. **81**, 1301 (2009).

[21] T. Zhong and F. N. C. Wong, Nonlocal cancellation of dispersion in Franson interferometry, Phys. Rev. A **88**, 020103 (2013).

[22] Z. Zhang, J. Mower, D. Englund, F. N. Wong, and J. H. Shapiro, Unconditional Security of Time-Energy Entanglement Quantum Key Distribution Using Dual-Basis Interferometry, Phys. Rev. Lett. **112**, 120506 (2014).

[23] D. B. Leviton and B. J. Frey, Temperature-dependent absolute refractive index measurements of synthetic fused silica (2008).

[24] Corning, Corning smf-28 ull optical fiber (2000).

[25] C. Baker, Y. Lu, and X. Bao, Chromatic-dispersion measurement by modulation phase-shift method using a Kerr phase-interrogator, Opt. Express **22**, 22314 (2014).

[26] M. Sucbei and D. Kim, Reflectometric fiber dispersion measurement using a supercontinuum pulse source, IEEE Photonics Technol. Lett. **21**, 1262 (2009).

[27] T. Grosz, A. P. Kovacs, M. Kiss, and R. Szipocs, Measurement of higher order chromatic dispersion in a photonic bandgap fiber, Appl. Opt. **53**, 1929 (2014).